Biogeosciences

High-frequency variability of CO_2 in Grand Passage, Bay of Fundy, Nova Scotia

Rachel M. Horwitz[1,a], Alex E. Hay[1], William J. Burt[1,b], Richard A. Cheel[1], Joseph Salisbury[2], and Helmuth Thomas[1,c]

[1]Dalhousie University, Department of Oceanography, Halifax, Nova Scotia, Canada
[2]University of New Hampshire, Institute for the Study of Earth, Oceans, and Space, Durham, New Hampshire, USA
[a]currently at: Bedford Institute of Oceanography, Fisheries and Oceans Canada, Dartmouth, Nova Scotia, Canada
[b]currently at: University of British Columbia, Department of Earth, Ocean and Atmospheric Sciences,
Vancouver, British Columbia, Canada
[c]currently at: Helmholtz Centre Geesthacht, Institute of Coastal Research, Gessthacht, Germany

Correspondence: Rachel M. Horwitz (rmhorwitz@gmail.com)

Abstract. Assessing changes in the marine carbon cycle arising from anthropogenic CO_2 emissions requires a detailed understanding of the carbonate system's natural variability. Coastal ecosystems vary over short spatial and temporal scales, so their dynamics are not well described by long-term and broad regional averages. A year-long time series of $p CO_2$, temperature, salinity, and currents is used to quantify the high-frequency variability of the carbonate system at the mouth of the Bay of Fundy, Nova Scotia. The seasonal cycle of $p CO_2$ is modulated by a diel cycle that is larger in summer than in winter and a tidal contribution that is primarily M2, with amplitude roughly half that of the diel cycle throughout the year. The interaction between tidal currents and carbonate system variables leads to lateral transport by tidal pumping, which moves alkalinity and dissolved inorganic carbon (DIC) out of the bay, opposite to the mean flow in the region, and constitutes a new feature of how this strongly tidal region connects to the larger Gulf of Maine and northwest Atlantic carbon system. These results suggest that tidal pumping could substantially modulate the coastal ocean's response to global ocean acidification in any region with large tides and spatial variation in biological activity, requiring that high-frequency variability be accounted for in assessments of carbon budgets of coastal regions.

1 Introduction

Oceanic uptake of anthropogenic carbon dioxide (CO_2) moderates the rise of atmospheric CO_2 concentrations and leads to changes in the ocean carbon cycle. CO_2 uptake acidifies the oceans, potentially altering ecosystems and leading to adverse effects for the societies and industries that depend on them. Assessing the vulnerability of these resources to long-term change in ocean acidification requires a detailed understanding of the carbonate system's natural variability that any anthropogenic trend may add to or alter. Coastal ecosystems vary on shorter temporal and spatial scales than the shelf or open ocean so predicting how they may change under future climate scenarios is more difficult and requires an understanding of the system's high-frequency components.

The Bay of Fundy (Fig. 1, inset) is an approximately 200 km long, 50 km wide, 75 m deep bay that extends northeastward into Canada from the Gulf of Maine in the northwest Atlantic Ocean. The regional circulation flows southward along the Scotian Shelf as the Nova Scotia Current, follows the coastline around southern Nova Scotia to enter the southern side of the Bay of Fundy, and exits the bay along the northern side to join the Eastern Maine Coastal Current in the Gulf of Maine (Bigelow, 1927; Greenberg, 1983; Hannah et al., 2001; Pettigrew et al., 2005; Dever et al., 2016). The mean circulation and water properties of the Gulf of Maine and the Nova Scotia Current are well described (e.g., Smith, 1989; Smith et al., 2001; Hannah et al., 2001; Houghton and Fairbanks, 2001; Aretxabaleta et al., 2008;
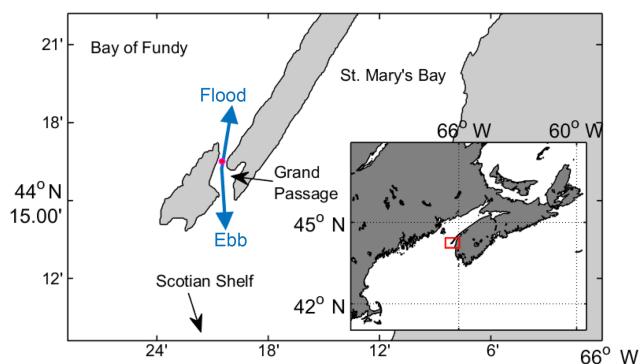
Figure 1. Map of Grand Passage, which cuts through a peninsula in southwest Nova Scotia. Instrument location indicated by the pink dot. Flood and ebb tide flow directions shown in blue arrows. Inset: map of the region with the red box indicating the field site at the mouth of the Bay of Fundy.

Gledhill et al., 2015; Dever et al., 2016). Within the bay the mean flow recirculates cyclonically around the outer Bay of Fundy (Aretxabaleta et al., 2008). The geometry of the basin makes it resonant with the M2 tidal frequency and generates the highest tidal range in the world, over 16 m at the head of the bay (Garrett, 1972; Greenberg, 1983). Turbulence from the fast tidal flows keeps much of the basin well mixed, while the deeper regions of the outer bay develop seasonal stratification. The largest freshwater source to the bay is the St. John River, on the northern coast, so owing to river plume dynamics and the general circulation of the region, this river water primarily propagates along the northern coast, into the Gulf of Maine.

Seasonal and inter-annual variability in air–sea CO_2 flux, along with the key carbon cycling processes, have been documented both upstream from the Bay of Fundy on the Scotian Shelf (e.g., Shadwick et al., 2010, 2011; Thomas et al., 2012; Craig et al., 2015) and downstream in the Gulf of Maine (Salisbury et al., 2009; Vandemark et al., 2011). Within the bay, salt marshes have been shown to be weak emitters of CO_2 to the atmosphere (Magenheimer et al., 1996), but these results might not be representative of fully submerged regions. Basin-wide estimates of CO_2 fluxes have come as part of larger-scale coastal studies where the Bay of Fundy is included as part of the Gulf of Maine region. Using historical pCO_2 data and satellite algorithms, Signorini et al. (2013) identified the Gulf of Maine as a weak source of CO_2 to the atmosphere. In contrast, results from a coupled biogeochemical-circulation model indicate the Gulf of Maine to be a relatively strong sink of CO_2 compared to surrounding areas (Cahill et al., 2016).

The coastal carbon budget and thus the rate at which alkalinity will be able to buffer future ocean acidification depend on the exchange processes between coastal and open oceans. In shallow marshy estuaries, tidal budgets have been estimated for oxygen from dissolved oxygen measurements

(Nidzieko et al., 2014) and for carbon from a linear model based on pH and oxidation-reduction potential (Wang et al., 2016). However, to the best of our knowledge, the tidal transport of carbon in this macrotidal system, or far from large freshwater or nutrient sources, has never been addressed.

To investigate this issue, a year-long, high-frequency time series of pCO_2, temperature, salinity, and currents was measured via a cabled-to-shore platform in Grand Passage, a tidal channel at the mouth of the Bay of Fundy, Nova Scotia (Fig. 1). This location is ideal for tracing the main input of water into the Bay from the Scotian Shelf. We quantify carbonate system variability on hourly to seasonal timescales, unravel the interaction between the daily and tidal cycles, determine the phase relationship between tidal currents and carbonate system variables, and estimate lateral transports by tidal pumping, which moves alkalinity and dissolved inorganic carbon (DIC) out of the bay, opposite to the mean flow in the region.

2 Measurements and data processing

Grand Passage is a narrow channel (1 km wide, 4 km long) separating Brier Island from Long Island at the end of the Digby Neck peninsula, which juts out into the mouth of the Bay of Fundy from the southwest corner of Nova Scotia (Fig. 1, inset). The tidal range is 5 to 6 m and peak tidal velocities range from 2 to 3 m s^{-1}.

2.1 Time series measurements

A year-long record of high-frequency measurements of pCO_2 (Fig. 2a), temperature (Fig. 2b), and pressure, 4 months of salinity (Fig. 2c), and 1 month of velocity data were collected via a cabled-to-shore observatory on a bottom frame that was deployed in approximately 10.5 m mean water depth (location indicated on Fig. 1).

The primary instrument for this experiment was a CONTROS HydroC CO_2 sensor, which uses non-dispersive infrared spectrometry (NDIR) to measure gas concentrations that have equilibrated across a hydrophobic membrane. The HydroC was calibrated by the manufacturer before and after deployment and has a resolution of < 1 µatm, an accuracy of ±1 %, and a response time of 65 s at 15 °C and 70 s at 5 °C. All field measurements fell within the calibrated measurement range of 200–1000 µatm. The HydroC was mounted 1 m above the sea floor and cabled to shore for continuous power and data transfer. It recorded pCO_2 every 1 s from March 2015 to April 2016. The instrument was zeroed every 64 min until 16 June 2015 and every 735 min for the remainder of the experiment. During zeroing the gas stream is isolated from the membrane and CO_2 is removed. Zero-channel values indicate no sensor drift over the deployment period. Following zeroing, partial pressure re-equilibrated
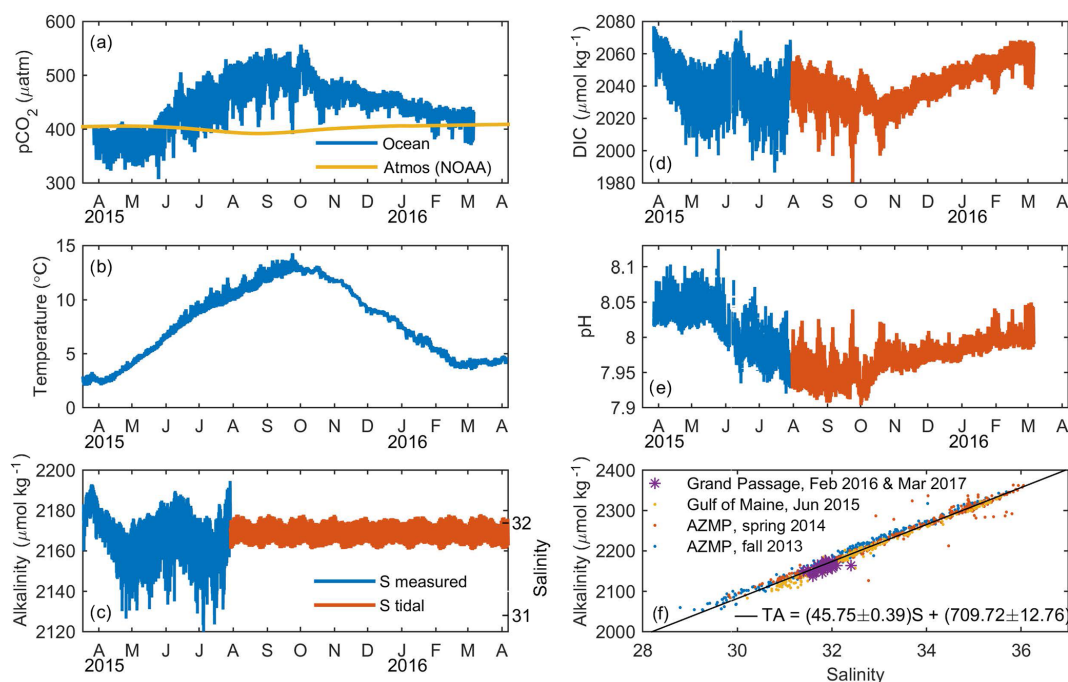
Figure 2. (a–c) Measured variables and **(d, e)** time series generated from the carbonate system equilibrium solution for data shown in **(a–c)**. **(a)** $p\mathrm{CO_2}$ in Grand Passage (blue) and NOAA's weekly atmospheric zonal average for 44–45° N (yellow). **(b)** Temperature. **(c)** Salinity (right y axis) and alkalinity (left y axis) from periods with salinity data (blue) and generated from a tidal prediction when measurements were not available owing to instrument failure (orange). **(d)** DIC. **(e)** pH. **(f)** Alkalinity vs. salinity from bottle samples at the Grand Passage field site in 2016 and 2017 (purple) as well as from the Scotian Shelf via the Atlantic Zone Monitoring Program (AZMP) in 2013 (blue) and 2014 (orange) and the Gulf of Maine in 2015 (yellow). Linear regression (black) used to generate alkalinity shown in **(c)**.

over roughly 1 h and data from these periods were omitted from analyses.

A CTD (conductivity, temperature, and depth instrument) was collocated with the HydroC and recorded salinity, temperature, and pressure data every 30 s from March through July 2015. The CTD was recovered and redeployed to record data every 60 s until April 2016. The conductivity sensor biofouled soon after redeployment so only temperature and pressure are available for the second half of the experiment.

Salinity measurements were despiked and a linear drift of 0.41 over the first deployment period was removed. The drift was determined by matching the final measured tidal cycle to the initial tidal cycle values from the redeployment of the CTD on the following day (prefouling). Salinity was estimated for the remainder of the year using tidal harmonic analysis (Pawlowicz et al., 2002; Codiga, 2011) of the available 4 months of data. Salinity variation at frequencies lower or higher than the tidal harmonics is absent from the latter part of the data set, but does not change the final results of this work because the direct effect of salinity and alkalinity (Sect. 2.4) variation is subtracted from the DIC$_{ex}$ variable (Sect. 3.2) used for quantitative analyses.

An RDI Workhorse 600 kHz ADCP (Acoustic Doppler Current Profiler) was deployed nearby, in approximately 27 m water depth, for part of the experimental period. The

upward-looking ADCP recorded velocity in 0.5 m bins at 2 Hz from 8 to 26 April 2015.

All time series variables were low-pass filtered with a cutoff period of 5 min and then subsampled at a 5 min interval.

2.2 Bottle samples

Bottle samples were collected from the ferry wharf on the west side of Grand Passage over 2 days in February 2016. On 16 February 2016, 12 bottles were filled hourly from 07:30 to 18:30 local time, using a Niskin bottle cast off the wharf, from 0.5 to 1 m below the surface. On 17 February 2016, 22 samples were collected half-hourly from 07:00 to 18:00. The Niskin bottle was used for seven samples, until it broke. Later samples were collected from the adjacent shore, approximately 5 m from shore in 1.5 m water depth, from 0.5 m below the surface. On 18 March 2017, 15 bottle samples were collected between 09:00 and 13:00 ADT (UTC−3) via Niskin casts off the *Nova Endeavor*, alternating between the center, east, and west sides of Grand Passage across a transect adjacent to the cabled instruments.

Bottle samples for total alkalinity analysis were poisoned with a supersaturated mercuric chloride solution to halt biological activity and stored for later analysis. Total alkalinity was analyzed by potentiometric titration on a Versatile In-

strument for the Determination of Titration Alkalinity (VIN-DTA 3C). Analytical methods were based on Dickson et al. (2007), including the use of certified reference materials for regular instrument calibration.

2.3 Other data sources

Hourly wind speeds and daily precipitation for the entire experiment period were obtained from the Environment and Climate Change Canada (ECCC) weather station on Brier Island, on the western side of Grand Passage (http://climate.weather.gc.ca/climate_data/hourly_data_e.html?StationID=10859, last access: 14 January 2019).

Atmospheric CO_2 concentrations were obtained from the NOAA Greenhouse Gas Marine Boundary Layer Reference data product (Dlugokency et al., 2015). At the time of data processing, $\sim$ weekly (1/48 of a year) values were available through 2015 for both zonal average values for 44–45° N and global average values. Monthly global average values were additionally available through September 2016 (ftp://aftp.cmdl.noaa.gov/products/trends/co2/co2_mm_gl.txt, last access: 14 January 2019) so estimates for 44–45° N were constructed for January–April 2016 by adding the difference between the zonal and global values for 2013–2015, averaged by calendar week, to the global values for 2016.

Alkalinity and salinity data from the Gulf of Maine shown in Fig. 2f and used in Eq. (1) were obtained from the NOAA Ocean Acidification Program (Salisbury, 2017).

Alkalinity and salinity data from the Scotian Shelf shown in Fig. 2f and used in Eq. (1) were collected at all stations as part of the Atlantic Zone Monitoring Program (AZMP) (Fisheries and Oceans Canada, 2013–2014) in Fall 2013 and Spring 2014. Samples were collected and processed following the methods described in Shadwick and Thomas (2014) for the 2007 AZMP data set.

2.4 Estimating alkalinity from salinity

A linear relationship between salinity, S, and alkalinity, TA, (Fig. 2f) was calculated with data from the bottle samples collected at the field site in February 2016 ($n = 34$) and March 2017 ($n = 15$), from the AZMP Fall 2013 ($n = 357$) and Spring 2014 ($n = 467$) cruises, and from the Gulf of Maine in 2015 ($n = 286$).

$$TA = (45.75 \pm 0.39)S + (709.72 \pm 12.76) \tag{1}$$

The Grand Passage data cover a small ($< 1\Delta PSU$) salinity range so a regression from only the Grand Passage field site was not robust. The Grand Passage salinity–alkalinity relationship was not a priori expected to be identical to the data collected 10 to 200 km offshore in the Scotian Shelf and Gulf of Maine regions, but Fig. 2f shows there is no significant change in the water mass end members between those regions, which are up- and downstream of Grand Passage in

the regional circulation pattern. A time series of alkalinity (Fig. 2c) is calculated from salinity using Eq. (1).

2.5 Calculating DIC

DIC concentration and pH (Fig. 2d, e) for the carbonate system at equilibrium were calculated from measurements of $p\mathrm{CO}_2$, salinity, alkalinity, and temperature, with constants following Dickson and Millero (1987) and Weiss (1974). We used the MATLAB code from van Heuven et al. (2011) for the CO2SYS implementation from Lewis and Wallace (1998) of the equations for carbonate equilibria.

3 Results and discussion

3.1 Seasonal evolution of carbonate system variables

Grand Passage connects two adjacent embayments, St. Mary's Bay and the Bay of Fundy, and because the water properties in these embayments can differ, the strong semi-diurnal (M2) tide causes tidal period variability in the carbonate system. $p\mathrm{CO}_2$ varies on annual, daily, and tidal timescales, and the magnitude of the daily and tidal signals also changes with the season. The seasonal evolution of $p\mathrm{CO}_2$ (Fig. 2a) is dominated by the effect of temperature (Fig. 2b), rising in summer and declining in winter, while biological processes only modulate this cycle. $p\mathrm{CO}_2$ ranges from a minimum of 307 µatm in spring 2015 up to a maximum of 557 µatm in early fall, with daily and M2 period variation of 32 and 10 µatm, respectively. In November, the daily range drops to 11 µatm and $p\mathrm{CO}_2$ decreases throughout the winter. Final measured values in March 2016 were 30 µatm higher than the those measured the previous spring, owing to the difference in water temperature.

Temperature (Fig. 2b) has a strong seasonal cycle, increasing from 2 °C in April 2015 up to 14 °C in September. Temperature decreases from October 2015 through March 2016, when it reaches an annual minimum of 3.5 °C, 1.5° higher than the previous springtime minimum. The ranges of daily and M2 tidal variation are 0.35 and 0.7 °C, respectively, in the summer and 0.1 and 0.15 °C during fall through spring.

The salinity (Fig. 2c, right axis) average for our March–July period of data availability was 31.9 with a 0.18 tidal variation and no daily signal. Salinity was not correlated with local wind or precipitation. Alkalinity mean and tidal variation were 2177 and 8.24 µmol kg^{-1}, respectively, based on the linear relationship between salinity and alkalinity measured with bottle samples (Fig. 2f and Sect. 2.4).

The in situ $p\mathrm{CO}_2$ value is important because it determines the air–sea flux of CO_2, but is not an ideal variable to assess biogeochemical carbonate dynamics because of its dependence on temperature and alkalinity, which obfuscate the biological processes. DIC (Fig. 2d) does not have a strong temperature dependence so it better depicts the biological DIC variation. DIC declines steeply during the spring bloom
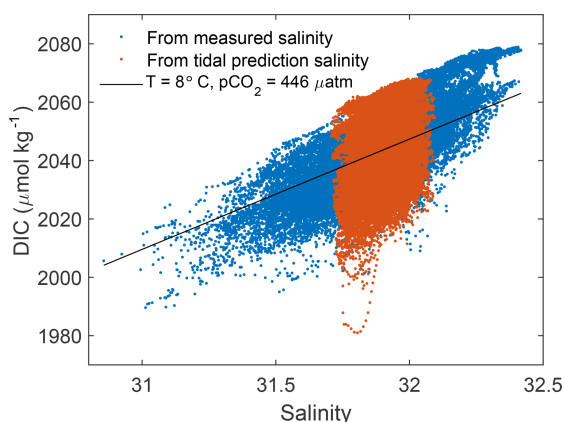
Figure 3. DIC vs. salinity for measured (blue) and tidal reconstruction (orange) carbonate system solutions. DIC at fixed $p\text{CO}_2$ (446 µatm) and temperature (8 °C) (black) is subtracted from observed DIC to create DIC_{ex}.

Figure 4. (a) DIC_{ex} for a calendar year with local time of day indicated by color. The time variation of the resulting DIC_{ex} is meaningful, while the total value depends on the specific choice of fixed $p\text{CO}_2$ used for the computation. **(b)** DIC_{ex} (color) for each hour of the day over a calendar year.

and then increases though the winter. During the spring bloom and throughout the summer there is a large daily range in DIC. In October, daily variability shrinks, and DIC increases steadily throughout the winter. pH varies as an approximate inverse of $p\text{CO}_2$. pH has an average value of 8.01 ($= -\log_{10}\langle[\text{H}^+]\rangle$) and daily and M2 variation are equivalent to changes in pH of 8 to 8.03 and 8 to 8.01, respectively.

3.2 Unraveling daily and tidal cycles of biogeochemically driven changes in DIC

In order to isolate the biogeochemically mediated changes in DIC from the variability due to purely physical processes, we define the variable "excess DIC" as the DIC remaining after the concentration expected from the physical mixing of water masses of different salinities and alkalinities has been subtracted. The DIC dependence on salinity and alkalinity, DIC_{mix}, is estimated numerically with CO2SYS using fixed values of $p\text{CO}_2$ and temperature. DIC_{mix} includes both a salinity-dependent component and a background constant that depends on $p\text{CO}_2$ and temperature. The mean $p\text{CO}_2$, 446 µatm, and temperature, 8 °C, for the deployment period are chosen for the calculation. DIC_{ex} is calculated by subtracting DIC_{mix} from the full (observed) DIC, DIC_{obs} (Fig. 3).

$$\text{DIC}_{ex} = \text{DIC}_{obs} - \text{DIC}_{mix}$$
$$\text{where} \quad \text{DIC}_{mix} = \text{DIC}(p\text{CO}_2 = 446, \text{T} = 8, S, \text{TA}) \quad (2)$$

Only the time variation of the resulting DIC_{ex} is meaningful, not the absolute value. This time variation is not sensitive to the choice of fixed $p\text{CO}_2$ and temperature from within the ranges typical of this field site. The relationship between $p\text{CO}_2$ and DIC that is captured in DIC_{ex} is unchanged over the small natural range of alkalinity in this region, so DIC_{ex}
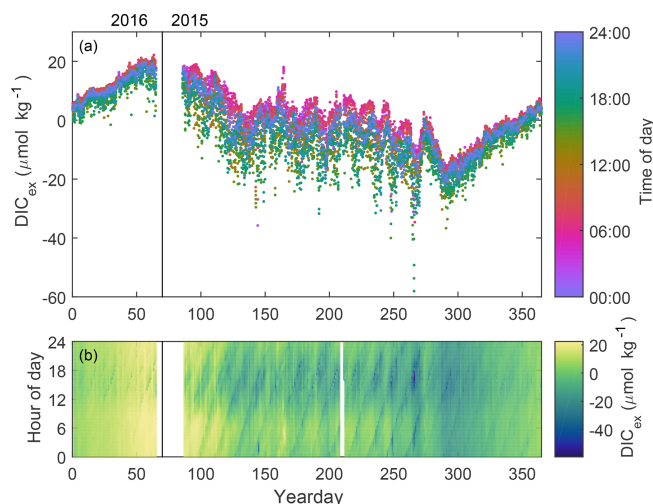
is not sensitive to the choice of a measured, tidal harmonic, or even constant salinity estimate. DIC_{ex} is presumed to be predominantly biogeochemically driven, but also includes any changes in DIC due to air–sea exchange, which we could not calculate on daily timescales, but are shown to be small on weekly timescales in Sect. 3.5.

DIC_{ex} (Fig. 4a) decreases rapidly April and May due to the spring bloom and more gradually over the summer, as explained by Craig et al. (2015). Following a decline in October (yearday 270–290) suggestive of a fall bloom, DIC_{ex} increases steadily through fall and winter. The daily cycle of DIC_{ex} is evident throughout the year when highlighted by the use of color to indicate local time of day in Fig. 4a. Daily maxima occur in early morning ($\sim 06{:}00$, pink dots) following nighttime respiration and minima in late afternoon ($\sim 17{:}00$, green dots) following the peak hours of sunlight and photosynthesis. This cycle is shifted several hours earlier than the one reported on the Scotian Shelf by Thomas et al. (2012). The daily range of DIC_{ex} is approximately 3 times as large in summer as in winter, consistent with higher summer sunlight supporting higher phytoplankton growth.

The solar and tidal cycles combine to create a fortnightly cycle (visible in Fig. 4a, but more clear in Fig. 4b). This beating pattern in the time series is due to the difference between the 12.42 h M2 tidal and 24 h diel periods. Mathematically, this effect is identical to a spring–neap tidal variation, but here the daily cycle is due to solar insolation, rather than the solar gravitational force. The diagonal banding pattern in Fig. 4b shows the M2 tide progressing 50 min later each day. The daily morning peak and afternoon low appear as broad horizontal stripes and are most visible for yeardays 100–275. A similar daily pattern has been observed on the

Scotian Shelf (Thomas et al., 2012), but no tidal signal was detected there. The pulsing of the strength of the morning high and afternoon low is due to the coincidence of an M2 maximum or minimum with the time of the daily maximum or minimum.

The overlapping daily and tidal cycles apparent in Fig. 4 can be separated and quantified by spectral analysis. Power spectral densities of DIC$_{ex}$, $P_{DIC_{ex}}(f)$ for frequency f, were calculated by Welch's method on detrended time series for each month with eight approximately week-long Hamming windowed segments with 50 % overlap. The position of peaks in spectra of month-long DIC$_{ex}$ time series (Fig. 5a) identify the frequencies with the greatest variability, and the area under each peak equals the contribution of that frequency to the total signal variance. These February and August examples show a large daily peak and a slightly smaller M2 tidal peak for both months, and they show that DIC$_{ex}$ is more variable in August than February at all frequencies. The third and fourth peaks visible in Fig. 5a are harmonics of the 24 h and M2 frequencies and do not substantially contribute to the total signal variance. The variance of DIC$_{ex}$ at the 24 h and M2 frequencies are calculated from the area under the spectra using a five-point peak width, $\sigma_{DIC_{ex}}^2 = \sum P_{DIC_{ex}}(f)\Delta f$. The total DIC$_{ex}$ variance is 10 times higher in August than in February but in both seasons the daily and M2 frequencies represent the majority of the variability: 56 % (56 %) and 19 % (7 %), respectively, of the total DIC$_{ex}$ signal variance in August (February).

The strengths of M2 and daily cycles in DIC$_{ex}$ evolve with the season (Fig. 5b). The range of DIC$_{ex}$ variation at a particular frequency is defined as $2A$ for amplitude A, i.e., the "peak-to-trough" difference of a sine wave. The rms value of a sinusoid equals $A/\sqrt{2}$, so the range of the daily or tidal DIC cycle equals $2 \times \sqrt{2} \times \sigma_{DIC_{ex}}$. Months from April through September have a similar size daily signal near 15 µmol kg^{-1}, with lower values throughout the winter. The tidal variation is always smaller than the daily variation but is also generally larger in summer and smaller in winter. However, unlike the daily signal, June and July have smaller tidal variation than the shoulder months of April, May, August, and September. Changes in the strength of the tidal signal reflect changes in spatial gradients of DIC$_{ex}$, presumably owing to season fluctuations in the spatial variation of biological activity.

3.3 Tidal phasing

The relationships between the tidal flow and DIC$_{ex}$, temperature, salinity and alkalinity, and H$_{ex}^+$ are depicted in Fig. 6 for April 2015, when velocity measurements were available. This tidal-phase information complements the daily cycle of DIC$_{ex}$ emphasized in Fig. 4a.

Salinity and corresponding alkalinity (Fig. 6a) are lowest during late flood and highest between maximum ebb and early flood (see ebb and flood directions on Fig. 1). Salinity values are lower during flood compared to those on ebb,
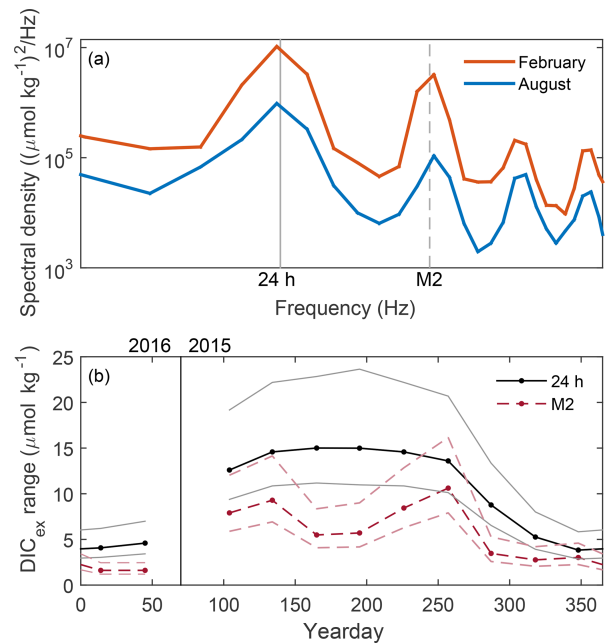

Figure 5. (a) Spectra of DIC$_{ex}$ in February (blue) and August (orange). **(b)** DIC$_{ex}$ range over daily (black, solid) and M2 (red, dashed) cycles for each month of the year. Amplitude determined from area beneath peaks in spectra, such as examples shown in **(a)**. The 95 % confidence intervals are shown in lighter colors.

which indicates that the water from St. Mary's Bay/Scotian Shelf that enters the Bay of Fundy through Grand Passage each flood tide is fresher than what exits during ebb. This tidal asymmetry in salinity holds for all months of the year.

Temperature (Fig. 6b) is lowest in late flood and peaks a short time later during early ebb, and overall the water is colder during flood than during ebb. Unlike the salinity asymmetry, the temperature asymmetry changes sign with the seasons. The shallower St. Mary's Bay is more sensitive to surface heat fluxes than the deeper Bay of Fundy, so it is warmer in spring and summer and colder in fall and winter. As a result, the oscillating tides move heat into the Bay of Fundy half of the year and out half of the year.

DIC$_{ex}$ (Fig. 6c) peaks at low slack and the lowest values occur during late flood and early ebb. H$_{ex}^+$ (Fig. 6d) also peaks at low slack and has the lowest values during early ebb. This pattern suggests lower net community production (NCP) in the bay than on the shelf, likely a result of a stronger spring bloom on the shelf than in the bay, which is advected by the mean currents around southern Nova Scotia. Smaller-scale spatial variation in nutrient or light availability owing to different water depths or mixing rates could also contribute to different growth rates on the two sides of Grand Passage.
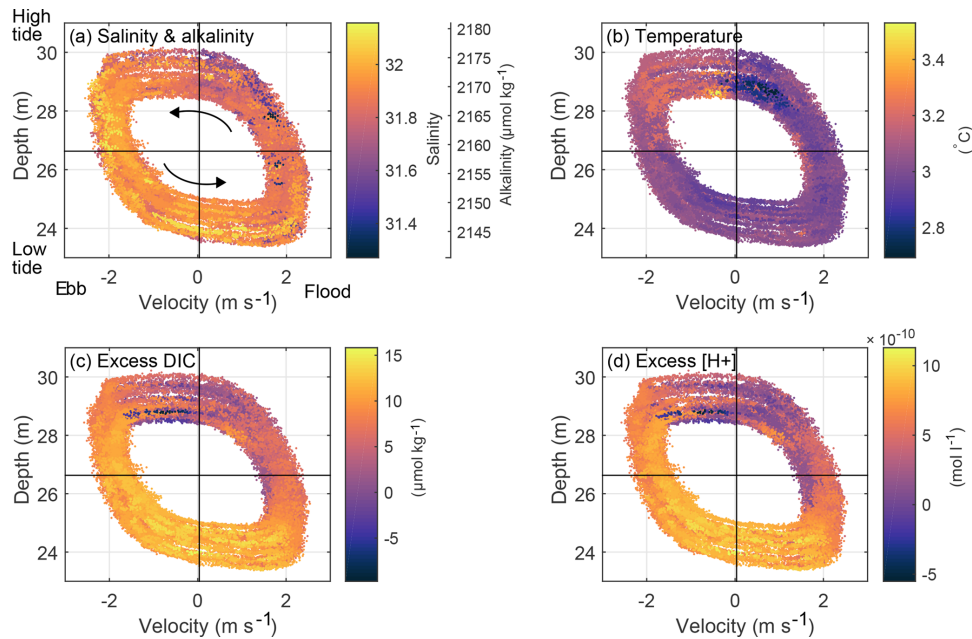
Figure 6. The relationships between the tidal flow and **(a)** salinity and alkalinity, **(b)** temperature, **(c)** DIC_{ex}, and **(d)** H_{ex}^+ are depicted for April 2015, when velocity measurements were recorded. The phase of the tide is indicated by ADCP water depth on the y axis and depth-averaged along-channel velocity on the x axis (positive in flood direction, i.e., northward, into the Bay of Fundy), with mean values indicated by black lines. Phase progression is counterclockwise, shown by arrows in **(a)**. Scalar concentration is indicated by color; for example, more yellow data points visible on the left side of **(a)** indicate higher salinity during ebb tide, when water is leaving the Bay of Fundy. The variation in position of the tidal ellipse between each pass of the tidal cycle reflects the changes in tidal range and maximum speed associated with the spring–neap cycle. For all variables shown by colors, 18 h high-pass-filtered values plus mean are plotted to visually highlight the M2 variability by eliminating the daily signal; the filtering is not used for data analyses. H_{ex}^+ is computed using the same method as DIC_{ex}, for $H^+ = 10^{-pH}$.

3.4 Lateral transport by tidal pumping

Transport of carbon through Grand Passage is driven both by net volume transport and by tidal pumping – oscillatory tides moving water masses with different properties back and forth on each tidal cycle. Water volume flux per meter of channel width, q (m² s⁻¹) $= \overline{u}h$, for water depth h (m) and depth-averaged velocity $\overline{u}$ (m s⁻¹) can be decomposed into a time-mean ($\langle \rangle$) and fluctuating ($'$) part, $q = \langle q \rangle + q'$. By definition, there is no net water volume transport by the time-varying volume flux used to calculate tidal pumping. The fluctuations in volume transport (Fig. 7a) that drive tidal pumping vary in magnitude over the spring–neap cycle, but return to zero each tidal cycle.

Any correlation between the tidal water volume flux, q', and fluctuations in conserved carbonate system concentration variables, $S' = S - \langle S \rangle$ (g m⁻³ or mol m⁻³), leads to a scalar flux by tidal pumping, $Q_{pump}^S = \langle q'S' \rangle$ (mol m⁻¹ s⁻¹ or g m⁻¹ s⁻¹), when averaged over timescales longer than a tidal cycle. Salinity is nearly vertically uniform at this field site (Razaz et al., 2019), and we assume DIC is also vertically uniform because the vertical mixing timescale is much shorter than the timescale of gas exchange owing to the high turbulence in the Bay of Fundy (Appendix A1), i.e.,

$\int_0^h S(z)u(z)\mathrm{d}z = S\overline{u}$. Fluctuations of the conserved variable that are not correlated with fluctuations in water volume flux, such as the daily or seasonal cycles shown in Fig. 4a, are in S' but do not contribute to Q_{pump}^S because they are not correlated with q'.

Cumulative along-channel transports, M (m³, mol, or g C), of water volume, alkalinity, and DIC_{ex} (Fig. 7) are calculated by multiplying q', $q'TA'$, and $q'DIC_{ex}'$ by the width ($w = 800$ m) of Grand Passage and integrating in time, t. We assume spatial uniformity of water properties across the section.

$$M_S(t) = \int_0^t q'S'w\mathrm{d}t \tag{3}$$

The fluctuating water volume flux, q', used to compute these transports is a tidal harmonic solution based on a fit to the month of ADCP data from April 2015. The harmonic fit represents 93 % of the observed variability (i.e., $R = 0.97$) in water volume flux. By contrast, the tidal harmonic fit to the 4 months of salinity measurements (Sect. 2.1) is not well correlated with the observations ($R = 0.35$), owing to the non-sinusoidal shape of the salinity signal as well as longer period variability. Due to this poor fit, alkalinity fluxes are not com-
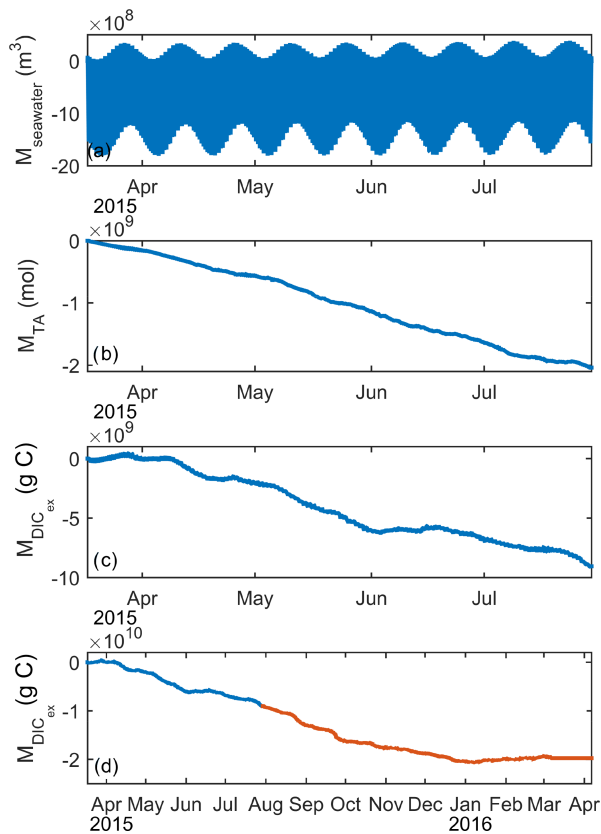
Figure 7. Cumulative along-channel transport since the start of the deployment period by tidal pumping of **(a)** water volume, **(b)** alkalinity, and **(c)** DIC$_{ex}$ for March–July 2015 and **(d)** DIC$_{ex}$ for the full year; orange color indicates period not shown in **(a)**–**(c)**. Salt or alkalinity fluxes are not computed for the full year because fluxes from the constructed tidal salinities will only reflect the mean trend already seen in Fig. 7b and not contain changes in phase or magnitude that might occur in the fall or winter.

puted for the period without direct salinity measurements. DIC$_{ex}$ is not affected by the salinity, as described in Sect. 3.2, so DIC$_{ex}$ transport is calculated for the full year.

For the first half of 2015, salt and alkalinity (Fig. 7b) are pumped southward, out of the Bay of Fundy by the tides. DIC$_{ex}$ (Fig. 7c) also has net negative (southward) transport over this period, but has shorter periods of near-zero or positive transport in March, mid-April, and early June.

Tidal pumping for DIC$_{ex}$ is also calculated for the second half of the deployment year (Fig. 7d) and continues the negative trend until January 2016, when the flux becomes slightly positive for the last 2 months of the measurement period. Salinity from a seasonal climatology (e.g Richaud et al., 2016; Signorini et al., 2013) suggests that the sign of the lateral salinity gradient is the same all year, indicating that the sign of the alkalinity flux will stay the same throughout the year.

Notably, these transports move alkalinity and DIC$_{ex}$ in the opposite direction of the mean flow of the region, which fol-

lows the coast clockwise around southwestern Nova Scotia, moving northward into the Bay of Fundy near Grand Passage (e.g., Aretxabaleta et al., 2008). Within Grand Passage, salinity and alkalinity transport by tidal pumping is roughly 20 % of that by the mean volume flux through the channel (Appendix A2). The exact fraction may vary outside the channel, but the important point is that tidal pumping likely plays a first-order role in carbon transport budgets anywhere with large tides and spatial gradients in the biogeochemical water properties, including the entire width of the mouth of the Bay of Fundy.

While the mean volume transport through Grand Passage cannot be extrapolated to the full width of the Bay of Fundy, the tidal pumping term could plausibly apply over the eastern side of the mouth, where salinity gradients are positive into the bay. If the transport by tidal pumping is applied out to just 10 km from shore ($\sim$ 15 % of the width of the mouth of the bay), which is a $\sim$ 50 m deep region, the DIC$_{ex}$ transported out of the Bay of Fundy through lateral advection by tidal pumping would be 5×10^8 kg C in a year. This value is 3 times what is estimated to leave the Bay of Fundy by outgassing to the atmosphere if the Grand Passage air–sea fluxes (Sect. 3.5) applied over the whole bay.

3.5 Air–sea CO$_2$ flux

High-frequency variability in DIC$_{ex}$ is assumed to be driven by biological and biogeochemical processes, but air–sea flux plays a significant role on long timescales. We assess the importance of air–sea flux to the carbon budget by calculating weekly and annual fluxes, as well as the equivalent changes in DIC. Oceanic pCO$_2$ was lower than atmospheric pCO$_2$ (Fig. 2a) for the first 2 months of observations, April and May, and then rose and remained higher than atmospheric pCO$_2$ for the following 10 months, June through March, giving an annual net negative CO$_2$ flux (i.e., outgassing) at this site.

Atmospheric and oceanic CO$_2$ concentrations (Fig. 2a) and wind speed (Sect. 2.3) are used to calculate the flux of CO$_2$ between the atmosphere and ocean at the field site. Atmospheric and oceanic pCO$_2$ data were interpolated onto the hourly wind time base. Air–sea flux, F (mol m^{-2} s^{-1}), is calculated following Wanninkhof et al. (2009) Eq. (3), here using the convention that F is positive for a flux of gas from the atmosphere into the ocean.

$$F = -kK_0(p\text{CO}_{2\,\text{ocean}} - p\text{CO}_{2\,\text{air}}), \qquad (4)$$

where K_0 is the solubility of CO$_2$ (mol m^{-3} Pa^{-1}) and k (m s^{-1}) is gas transfer velocity. k (cm h^{-1}) can be represented well for wind speeds, U (m s^{-1}), below 15 m s^{-1} at Schmidt number $Sc = 660$ with the empirical formula (Wanninkhof et al., 2009, Eq. 37)

$$k_{660} = 0.24\langle U_{10}^2\rangle. \qquad (5)$$

U_{10} is the 10 m wind speed measured at the ECCC station on Brier Island. U_{10} was also computed as the difference between the air and water speeds (up to $\pm 2\,\text{m}\,\text{s}^{-1}$), which increased the air–sea flux estimates by approximately 5 %. Air–sea flux is initially computed on an hourly timescale to fully capture the quadratic wind-speed dependence, but only weekly (or longer) averages of F are robust owing to the weekly timescale of the available atmospheric $p\text{CO}_2$ data.

The average air–sea CO₂ flux at this site is $-4.6 \times 10^{-8}\,\text{mol}\,\text{m}^{-2}\,\text{s}^{-1}$, which is similar in magnitude to previous Gulf of Maine flux estimates, but with outgassing most of the year rather than the more even split between positive and negative fluxes reported at a deeper site (Vandemark et al., 2011) or for regional averages (Signorini et al., 2013; Cahill et al., 2016). If this gas exchange was spatially uniform over the Bay of Fundy (approx. $10^4\,\text{km}^2$), this air–sea flux would release 1.75×10^8 kg carbon ($= 1.45 \times 10^{10}$ mol) into the atmosphere per year.

The annual local flux is equivalent to a $-47\,\mu\text{mol}\,\text{kg}^{-1}$ change in DIC_{ex} (Eq. 6) when applied to 30 m water depth in Grand Passage over the year-long deployment.

$$\Delta \text{DIC}_{\text{air–sea}} = \frac{F_{\text{air–sea}}}{h}\Delta t \tag{6}$$

The weekly averaged flux is typically between 0 and $-1 \times 10^{-7}\,\text{mol}\,\text{m}^{-2}\,\text{s}^{-1}$, which is equivalent to up to $-2\,\mu\text{mol}\,\text{kg}^{-1}$ change in DIC_{ex} over a week. The maximum weekly value occurred in late September 2015 and was $-2 \times 10^{-7}\,\text{mol}\,\text{m}^{-2}\,\text{s}^{-1}$, yielding a $-4\,\mu\text{mol}\,\text{kg}^{-1}$ change in DIC_{ex} in 1 week.

3.6 Consideration of the local DIC budget

Observed DIC_{ex} variation is due to the difference between local (water column and sediment) net community production, local air–sea flux, and advective changes due to spatial gradients of biological production or air–sea flux (Appendix A3). Daily variation in DIC_{ex} can reasonably be attributed to the local time rate of change, and the tidal variation is likely advective. Longer cycles of variation could have both a local seasonal cycle and advective contributions from seasonal variation occurring weeks or months upstream.

We did not directly measure spatial gradients of DIC_{ex}, but can infer that the local along-channel gradient is positive (increasing northwards) from the observation that the highest and lowest values tend to occur near low and high slack water, respectively (Fig. 6). A positive along-channel DIC_{ex} gradient carried by a northward regional circulation decreases local DIC_{ex}.

DIC_{ex} returns near to its initial value over the full annual cycle (Fig. 4a) so the annual mean $\partial \text{DIC}_{\text{ex}}/\partial t$ is zero. The outgassing air–sea flux and along-channel advection both decrease DIC_{ex}, so to close the DIC budget (Eq. A6) the biologically driven change in DIC must be positive (NCP < 0) on average over the year, even though it is negative in the spring.

4 Conclusions

Open ocean carbon cycles can be described by annual and daily variations and taken to be uniform over large spatial scales. However, near the coast, ecosystems change markedly over short distances, so the dynamics of the carbonate system cannot be well described without resolving the spatial variation or capturing the effects of lateral advection.

In this work, we unravel tidal advection from the diel production and respiration cycles due to solar radiation and show that the tides pump both alkalinity and DIC out of the Bay of Fundy into the open ocean, opposite to the transport via the residual flow. This tidal pumping process, in contrast to any residual flow, does not result in a net transport of water, but can greatly enhance the exchange of passive scalars like DIC. In regions with strong tidal currents and spatial variation in biological activities, tidal pumping could substantially modulate the coastal ocean's response to global ocean acidification.

High-frequency measurements reveal previously unaccounted for tidal variations in the carbonate system, in addition to more precise quantification of the familiar daily cycles and annual blooms. These results are crucial prerequisites to a deeper understanding of coastal systems' resilience or vulnerability to anthropogenic change.

Appendix A

A1 Vertical mixing

In this highly turbulent, unstratified water column, the vertical mixing timescale (Eq. A1) is much shorter than the timescale of gas exchange (Eq. A2).

$$T_{mix} = \frac{h^2}{A_\nu} \sim \frac{h^2}{(\kappa u_* h/12)} = \frac{h}{\kappa u_*/8}$$

$$\approx \frac{25\,m}{0.4 \times 0.1\,m\,s^{-1} \times 0.125} = 5000\,s = 1.4\,h, \quad \text{(A1)}$$

$$T_{air-sea} = \frac{h}{k_{660}} \approx \frac{25\,m}{4 \times 10^{-5}\,m\,s^{-1}}$$

$$= 6.25 \times 10^5\,s = 7\,days, \quad \text{(A2)}$$

where h is total water depth at the ADCP site; the k_{660} value is the average from the data set; A_ν is eddy viscosity estimated as the mid-water-depth value of a cubic eddy viscosity profile for a logarithmic near-bed velocity profile and zero surface wind stress (e.g., Lentz, 1995); κ is the von Kármán constant; and u_* is the shear velocity with the value chosen from the Grand Passage site GP2 from McMillan et al. (2013), which is very close to the site of the present study.

A2 Mean volume transport

The mean volume flux, $\langle q \rangle$, is derived from both the mean depth-averaged along-channel velocity and the mean volume transport due to asymmetries in the tidal cycle $\langle q \rangle = \langle \overline{u}h \rangle = \langle \overline{u} \rangle \langle h \rangle + \langle \overline{u}'h' \rangle$. At the ADCP location, $\langle \overline{u} \rangle = 0.036\,m\,s^{-1}$ and $\langle h \rangle = 26.6\,m$, which are indicated by the solid black lines in Fig. 6, yielding $0.95\,m^2\,s^{-1}$ volume flux.

The position of the data points in Fig. 6 compared to the mean axes made by $\langle \overline{u} \rangle$ and $\langle h \rangle$ values shows that the water tends to be deeper during ebb than during flood. If the tide was a perfect standing wave (slack at high and low water, and maximum ebb and flood speeds occurring at the mean water depth), the shape of the depth-velocity points would form a circle. The mean volume flux due to this tidal asymmetry, $\langle \overline{u}'h' \rangle = -1.61\,m^2\,s^{-1}$, which is larger than, and in the opposite direction of, the volume flux by the mean depth-averaged velocity.

Assuming spatial uniformity over the channel width, the volume flux driven by the mean depth-averaged velocity applied to the mean salinity of 31.9 yields a salt flux of $2.3 \times 10^4\,kg\,s^{-1}$, and the volume flux driven by tidal asymmetry generates a salt flux of $-4.0 \times 10^4\,kg\,s^{-1}$.

The salt flux driven by total $\langle q \rangle$ from both components is $-1.6 \times 10^4\,kg\,s^{-1}$, which is 5 times the salt flux by tidal pumping shown in Fig. 7. However, the mean velocity and especially the phase lag between the tide depth and velocity is generated by friction and therefore sensitive to the specific channel geometry (e.g., Geyer and MacCready, 2014) and may vary across the mouth of the Bay of Fundy.

A3 Budget for biological DIC production

The change in observed DIC_{ex} is given by

$$\frac{\partial DIC_{ex}}{\partial t} = \frac{\partial DIC_{bio}}{\partial t} + \frac{\partial DIC_{air-sea}}{\partial t}. \quad \text{(A3)}$$

Biology and air–sea exchange both drive local changes in time, and both could potentially have changes in time due to advection of spatial gradients, which is what we (almost definitely) observe over the tidal cycle. For example,

$$\frac{\partial DIC_{bio}}{\partial t} = \frac{\partial DIC_{bio,local}}{\partial t} - u\frac{\partial DIC_{bio}}{\partial x}, \quad \text{(A4)}$$

where x is the along-channel distance and $\partial DIC_{bio,local}/\partial t$ corresponds to local carbon consumption (i.e., equal to $-NCP$). So in total

$$\frac{\partial DIC_{ex}}{\partial t} = \frac{\partial DIC_{bio,local}}{\partial t} + \frac{\partial DIC_{air-sea,local}}{\partial t} - u\frac{\partial DIC_{bio}}{\partial x}$$

$$- u\frac{\partial DIC_{air-sea}}{\partial x}. \quad \text{(A5)}$$

If we assume the air–sea flux is spatially uniform, $u\frac{\partial DIC_{air-sea}}{\partial x} = 0$, then the change in observed DIC that is attributable to biological activity, DIC_{bio}, is given by

$$\frac{\partial DIC_{bio,local}}{\partial t} - u\frac{\partial DIC_{bio}}{\partial x} = \frac{\partial DIC_{ex}}{\partial t} - \frac{\partial DIC_{air-sea}}{\partial t}. \quad \text{(A6)}$$

References

Aretxabaleta, A. L., McGillicuddy, D. J., Smith, K. W., and Lynch, D. R.: Model simulations of the Bay of Fundy Gyre: 1. Climatological results, J. Geophys. Res.-Oceans, 113, C10027, https://doi.org/10.1029/2007JC004480, 2008.

Bigelow, H. B.: Physical oceanography of the Gulf of Maine, Bulletin of the U.S. Bureau of Fisheries, 40, 511–1027, 1927.

Cahill, B., Wilkin, J., Fennel, K., Vandemark, D., and Friedrichs, M. A. M.: Interannual and seasonal variabilities in air-sea CO_2 fluxes along the U.S. eastern continental shelf and their sensitivity to increasing air temperatures and variable winds, J. Geophys. Res.-Biogeo., 121, 295–311, https://doi.org/10.1002/2015JG002939, 2016.

Codiga, D. L.: Unified Tidal Analysis and Prediction Using the UTide Matlab Functions, Technical Report 2011-01, 59 pp., Graduate School of Oceanography, University of Rhode Island, Narragansett, RI, available at: http://www.po.gso.uri.edu/~codiga/utide/utide.htm (last access: 14 January 2019), 2011.

Craig, S. E., Thomas, H., Jones, C. T., Li, W. K., Greenan, B. J., Shadwick, E. H., and Burt, W. J.: The effect of seasonality in phytoplankton community composition on CO_2 uptake on the Scotian Shelf, J. Marine Syst., 147, 52–60, https://doi.org/10.1016/j.jmarsys.2014.07.006, 2015.

Dever, M., Hebert, D., Greenan, B., Sheng, J., and Smith, P.: Hydrography and Coastal Circulation along the Halifax Line and the Connections with the Gulf of St. Lawrence, Atmos. Ocean, 54, 199–217, https://doi.org/10.1080/07055900.2016.1189397, 2016.

Dickson, A. and Millero, F.: A comparison of the equilibrium constants for the dissociation of carbonic acid in seawater media, Deep-Sea Res. Pt. A, 34, 1733–1743, https://doi.org/10.1016/0198-0149(87)90021-5, 1987.

Dickson, A. G., Sabine, C. L., and Christian, J. R. (Eds.): Guide to best practices for ocean CO_2 measurements, PICES Special Publication 3, 191 pp., North Pacific Marine Science Organization, Sidney, British Columbia, Canada, 2007.

Dlugokency, E., Masarie, K., Lang, P., and Tans, P.: NOAA Greenhouse Gas Reference from Atmospheric Carbon Dioxide Dry Air Mole Fractions from the NOAA ESRL Carbon Cycle Cooperative Global Air Sampling Network, available at: http://www.esrl.noaa.gov/gmd/ccgg/mbl/data.php (last access: 14 January 2019), data Path: ftp://aftp.cmdl.noaa.gov/data/trace_gases/co2/flask/surface/ (last access: 14 January 2019), 2015.

Fisheries and Oceans Canada: Atlantic Zone Monitoring Program (AZMP), available at: http://www.meds-sdmm.dfo-mpo.gc.ca/isdm-gdsi/azmp-pmza/index-eng.html (last access: 14 January 2019), 2013–2014.

Garrett, C.: Tidal Resonance in the Bay of Fundy and Gulf of Maine, Nature, 238, 441–443, https://doi.org/10.1038/238441a0, 1972.

Geyer, W. R. and MacCready, P.: The Estuarine Circulation, Annu. Rev. Fluid Mech., 46, 175–197, https://doi.org/10.1146/annurev-fluid-010313-141302, 2014.

Gledhill, D. K., White, M. M., Salisbury, J., Thomas, H., Mlsna, I., Liebman, M., Mook, B., Grear, J., Candelmo, A. C., Chambers, R. C., Gobler, C. J., Hunt, C. W., King, A. L., Price, N. N., Signorini, S. R., Stancioff, E., Stymiest, C., Wahle, R. A., Waller, J. D., Rebuck, N. D., Wang, Z. A., Capson, T. L., Morrison, J. R., Cooley, S. R., and Doney, S. C.: Ocean and Coastal Acidification off New England and Nova Scotia, Oceanography, 28, 182–197, https://doi.org/10.5670/oceanog.2015.41, 2015.

Greenberg, D. A.: Modelling the Mean Barotropic Circulation in the Bay of Fundy and Gulf of Maine, J. Phys. Oceanogr., 13, 886–904, https://doi.org/10.1175/1520-0485(1983)013<0886:MTMBCI>2.0.CO;2, 1983.

Hannah, C. G., Shore, J. A., Loder, J. W., and Naimie, C. E.: Seasonal Circulation on the Western and Central Scotian Shelf, J. Phys. Oceanogr., 31, 591–615, https://doi.org/10.1175/1520-0485(2001)031<0591:SCOTWA>2.0.CO;2, 2001.

Houghton, R. and Fairbanks, R.: Water sources for Georges Bank, Deep-Sea Res. Pt. II, 48, 95–114, https://doi.org/10.1016/S0967-0645(00)00082-5, 2001.

Lentz, S. J.: Sensitivity of the Inner-Shelf Circulation to the Form of the Eddy Viscosity Profile, J. Phys. Oceanogr., 25, 19–28, https://doi.org/10.1175/1520-0485(1995)025<0019:SOTISC>2.0.CO;2, 1995.

Lewis, E. and Wallace, D. W. R.: Program Developed for CO_2 System Calculations, ORNL/CDIAC-105, Tech. rep., Carbon Dioxide Information Analysis Center, Oak Ridge National Laboratory, U.S. Department of Energy, Oak Ridge, Tennessee, 1998.

Magenheimer, J. F., Moore, T. R., Chmura, G. L., and Daoust, R. J.: Methane and carbon dioxide flux from a macrotidal salt marsh, Bay of Fundy, New Brunswick, Estuaries, 19, 139–145, https://doi.org/10.2307/1352658, 1996.

McMillan, J. M., Schillinger, D. J., and Hay, A. E.: Southwest Nova Scotia Resource Assessment, Volume 3: Acoustic Doppler Current Profiler Results, Tech. rep., Offshore Energy Research Association, available at: http://www.oera.ca/wp-content/uploads/2013/07/SWNT_Final-Report_Volume-3.pdf (last access: 14 January 2019), 2013.

Nidzieko, N. J., Needoba, J. A., Monismith, S. G., and Johnson, K. S.: Fortnightly Tidal Modulations Affect Net Community Production in a Mesotidal Estuary, Estuar. Coast., 37, 91–110, https://doi.org/10.1007/s12237-013-9765-2, 2014.

Pawlowicz, R., Beardsley, B., and Lentz, S.: Classical Tidal Harmonic Analysis Including Error Estimates in MATLAB using T_TIDE, Comput. Geosci., 28, 929–937, 2002.

Pettigrew, N. R., Churchill, J. H., Janzen, C. D., Mangum, L. J., Signell, R. P., Thomas, A. C., Townsend, D. W., Wallinga, J. P., and Xue, H.: The kinematic and hydrographic structure of the Gulf of Maine Coastal Current, Deep-Sea Res. Pt. II, 52, 2369–2391, https://doi.org/10.1016/j.dsr2.2005.06.033, 2005.

Razaz, M., Zedel, L., Hay, A. E., and Kawanisi, K.: Monitoring Tidal Currents in a Well-Mixed, Narrow Strait Using High-Frequency Acoustic Tomography, J. Geophy. Res., in review, 2019.

Richaud, B., Kwon, Y.-O., Joyce, T. M., Fratantoni, P. S., and Lentz, S. J.: Surface and bottom temperature and salinity climatology along the continental shelf off the Canadian and U.S. East Coasts., Cont. Shelf Res., 124, 165–181, https://doi.org/10.1016/j.csr.2016.06.005, 2016.

Salisbury, J., Vandemark, D., Hunt, C., Campbell, J., Jonsson, B., Mahadevan, A., McGillis, W., and Xue, H.: Episodic riverine influence on surface {DIC} in the coastal Gulf of Maine, Estuar. Coast. Shelf S., 82, 108–118, https://doi.org/10.1016/j.ecss.2008.12.021, 2009.

Salisbury, J. E.: Dissolved inorganic carbon, total alkalinity, pH, nutrients and other variables collected from profile and discrete sample observations using CTD, Niskin bottle, and other instruments from NOAA Ship Gordon Gunter off the U.S. East Coast during the East Coast Ocean Acidification (GU-15-04 ECOA1) from 2015-06-20 to 2015-07-23 (NCEI Accession 0159428), Version 2.2, NOAA National Centers for Environmental Information, Dataset, https://doi.org/10.7289/V5VT1Q40, 2017.

Shadwick, E. H. and Thomas, H.: Seasonal and spatial variability in the CO$_2$ system on the Scotian Shelf (Northwest Atlantic), Mar. Chem., 160, 42–55, https://doi.org/10.1016/j.marchem.2014.01.009, 2014.

Shadwick, E. H., Thomas, H., Comeau, A., Craig, S. E., Hunt, C. W., and Salisbury, J. E.: Air-Sea CO$_2$ fluxes on the Scotian Shelf: seasonal to multi-annual variability, Biogeosciences, 7, 3851–3867, https://doi.org/10.5194/bg-7-3851-2010, 2010.

Shadwick, E. H., Thomas, H., Azetsu-Scott, K., Greenan, B., Head, E., and Horne, E.: Seasonal variability of dissolved inorganic carbon and surface water pCO$_2$ in the Scotian Shelf region of the Northwestern Atlantic, Mar. Chem., 124, 23–37, https://doi.org/10.1016/j.marchem.2010.11.004, 2011.

Signorini, S. R., Mannino, A., Najjar, R. G., Friedrichs, M. A. M., Cai, W.-J., Salisbury, J., Wang, Z. A., Thomas, H., and Shadwick, E.: Surface ocean pCO$_2$ seasonality and sea-air CO$_2$ flux estimates for the North American east coast, J. Geophys. Res.-Oceans, 118, 5439–5460, https://doi.org/10.1002/jgrc.20369, 2013.

Smith, P. C.: Seasonal and Interannual Variability of Current, Temperature and Salinity off Southwest Nova Scotia, Can. J. Fish. Aquat. Sci., 46, s4–s20, https://doi.org/10.1139/f89-275, 1989.

Smith, P. C., Houghton, R. W., Fairbanks, R. G., and Mountain, D. G.: Interannual variability of boundary fluxes and water mass properties in the Gulf of Maine and on Georges Bank: 1993–1997, Deep-Sea Res. Pt. II, 48, 37–70, https://doi.org/10.1016/S0967-0645(00)00081-3, 2001.

Thomas, H., Craig, S. E., Greenan, B. J. W., Burt, W., Herndl, G. J., Higginson, S., Salt, L., Shadwick, E. H., and Urrego-Blanco, J.: Direct observations of diel biological CO$_2$ fixation on the Scotian Shelf, northwestern Atlantic Ocean, Biogeosciences, 9, 2301–2309, https://doi.org/10.5194/bg-9-2301-2012, 2012.

van Heuven, S., Pierrot, D., Rae, J. W. B., Lewis, E., and Wallace, D. W. R.: MATLAB Program Developed for CO$_2$ System Calculations, ORNL/CDIAC-105b, Carbon Dioxide Information Analysis Center, Oak Ridge National Laboratory, U.S. Department of Energy, Oak Ridge, Tennessee, https://doi.org/10.3334/CDIAC/otg.CO2SYS_MATLAB_v1.1, 2011.

Vandemark, D., Salisbury, J. E., Hunt, C. W., Shellito, S. M., Irish, J. D., McGillis, W. R., Sabine, C. L., and Maenner, S. M.: Temporal and spatial dynamics of CO$_2$ air-sea flux in the Gulf of Maine, J. Geophys. Res.-Oceans, 116, c01012, https://doi.org/10.1029/2010JC006408, 2011.

Wang, Z. A., Kroeger, K. D., Ganju, N. K., Gonneea, M. E., and Chu, S. N.: Intertidal salt marshes as an important source of inorganic carbon to the coastal ocean, Limnol. Oceanogr., 61, 1916–1931, https://doi.org/10.1002/lno.10347, 2016.

Wanninkhof, R., Asher, W. E., Ho, D. T., Sweeney, C., and McGillis, W. R.: Advances in Quantifying Air-Sea Gas Exchange and Environmental Forcing, Annu. Rev. Mar. Sci., 1, 213–244, https://doi.org/10.1146/annurev.marine.010908.163742, 2009.

Weiss, R.: Carbon dioxide in water and seawater: the solubility of a non-ideal gas, Mar. Chem., 2, 203–215, https://doi.org/10.1016/0304-4203(74)90015-2, 1974.